Spatiotemporal transcriptional dynamics of the cycling mouse oviduct

Elle C. Roberson[1], Anna M. Battenhouse[1], Riddhiman K. Garge[1], Ngan Kim Tran[1], Edward M. Marcotte[1], John B. Wallingford[1,*]

[1]Department of Molecular Biosciences, University of Texas at Austin, TX, USA 78712

ORCID: ECR, orcid.org/0000-0001-7466-7447; AMB, orcid.org/0000-0002-7455-9064; RKG, orcid.org/0000-0002-6774-0172; EMM, orcid.org/0000-0001-8808-180X; JBW, orcid.org/0000-0002-6280-8625

[*]Corresponding author information:
wallingford@austin.utexas.edu
Patterson Labs
University of Texas at Austin
2401 Speedway
Austin, TX 78712

Abstract

Female fertility in mammals requires iterative remodeling of the entire adult female reproductive tract across the menstrual/estrous cycle. However, while transcriptome dynamics across the estrous cycle have been reported in human and bovine models, no global analysis of gene expression across the estrous cycle has yet been reported for the mouse. Here, we examined the cellular composition and global transcriptional dynamics of the mouse oviduct along the anteroposterior axis and across the estrous cycle. We observed robust patterns of differential gene expression along the anteroposterior axis, but we found surprisingly few changes in gene expression across the estrous cycle. Notable gene expression differences along the anteroposterior axis included a surprising enrichment for genes related to embryonic development, such as Hox and Wnt genes. The relatively stable transcriptional dynamics across the estrous cycle differ markedly from other mammals, leading us to speculate that this is an evolutionarily derived state that may reflect the extremely rapid five-day mouse estrous cycle. This dataset fills a critical gap by providing an important genomic resource for a highly tractable genetic model of mammalian female reproduction.

Introduction

The adult mammalian female reproductive organs – ovary, oviduct, uterus, cervix, and vagina – hold an interesting position in mammalian physiology because they constantly and repeatedly engage in a complex remodeling process more commonly associated with development. With every menstrual or estrous cycle, fluctuations in ovarian steroid hormone secretion drive remodeling of these tissues, characterized by changes in proliferation, apoptosis, epithelial morphology, and fluid secretion (Brenner and West, 1975). However, while decades of research have revealed how these hormones fluctuate across the menstrual/estrous cycle in multiple mammals, we understand far less about the mechanisms by which these hormones drive cyclic tissue morphogenesis.

The oviducts are most well-known as the conduit between the ovary and uterus, but it is critical to note they also function as the site of fertilization and pre-implantation embryonic development (Coy et al., 2012; Coy and Yanagimachi, 2015; Stewart and Behringer, 2012). Interestingly, the oviducts display robust patterning along the anteroposterior axis, as the two major epithelial cell types – multiciliated cells (MCCs) and secretory cells – are differentially

32 enriched (Agduhr, 1927; Barton et al., 2020; Stewart and Behringer, 2012). At the anterior
33 oviduct close to the ovary, MCCs are highly enriched and responsible for capturing the ovulated
34 oocyte(s), while at the posterior close to the uterus, MCCs are very sparse and act as sperm
35 reservoirs (Suarez, 2016; Talbot et al., 1999). The reduced proportion of MCCs in the posterior
36 oviduct reflects the significant increase in the proportion of secretory cells, which are critical to
37 pre-implantation development (Coy and Yanagimachi, 2015). This anteroposterior pattern of the
38 mouse oviduct epithelium is known to be established early in postnatal life and requires signaling
39 from the underlying mesenchyme (Yamanouchi et al., 2010). How this pattern may change
40 across the estrous cycle is not known.
41 In many species, the cellular basis of morphogenesis of oviduct MCCs across the estrous
42 cycle was described *via* scanning electron microscopy studies decades ago (Brenner, 1969;
43 Shirley and Reeder, 1996; Verhage et al., 1973). In Rhesus monkeys, for example, anterior
44 oviduct epithelial cells are cuboidal at the beginning of the cycle, but then grow in height and
45 develop cilia at their apical surfaces as estrogen increases (Brenner, 1969). As estrogen decreases
46 and progesterone increases, the MCCs regress and de-ciliate (Brenner, 1969).
47
48 In mice, however, such cellular changes have not been thoroughly investigated, although
49 it was shown that the wet weight of oviducts, as well as RNA and protein concentration,
50 increases in the first half of the estrous cycle, and then subsequently decreases during the second
51 half (Bronson and Hamilton, 1971; Yamanouchi et al., 2010). More recently, there is evidence
52 that ciliary beat frequency changes in response to estrogen and progesterone (Bylander et al.,
53 2010; Shi et al., 2011). Perhaps surprisingly, while steroid hormone signaling in the oviduct is
54 crucial for female fertility (Herrera et al., 2020; Winuthayanon et al., 2015), we still lack a
55 comprehensive view of how cycling steroids impact cellular morphogenesis in the oviduct,
56 especially in the mouse.
57 A major hurdle to filling this knowledge gap is our very limited understanding of the
58 transcriptional dynamics that underlie cyclical morphogenesis in this tissue. Transcriptomic
59 approaches in human, swine, and bovine oviducts have investigated the impact of estrogen and
60 progesterone, and some studies have also explored anteroposterior patterning in humans and
61 bovine oviducts (Bauersachs et al., 2004; Cerny et al., 2015; Hess et al., 2013; Kim et al., 2018;
62 Sowamber et al., 2020). However, the majority of these studies have focused on either the

63 transcriptional response to fertilization and early embryo development or transcriptional
64 signatures associated with progression of high grade serous ovarian carcinoma in the oviduct.
65 The absence of a dynamic mouse oviduct transcriptome across the normal estrous cycle
66 represents a critical gap in our knowledge, especially given its potential utility as a model for
67 understanding mammalian fertility.
68 Here, we examined both the cellular changes and global transcriptional dynamics along
69 the length of the oviduct and across the estrous cycle. First, we provide quantitative data on the
70 density of MCCs along the anteroposterior axis of the oviduct and we show that MCCs do not
71 remodel across the estrous cycle in mice. In addition, we present 3' RNA-seq (Lohman et al.,
72 2016) data for the anterior (approximate infundibulum) and posterior (approximate isthmus)
73 oviduct at each stage of the estrous cycle. While transcript abundances vary strongly along the
74 anteroposterior axis, our analyses suggest the estrous cycle has a surprisingly limited impact on
75 transcription. Our data complement previous studies of transcriptional dynamics in the oviduct of
76 other mammals and provide an important new resource for genetic studies of oviduct function in
77 the mouse.
78
79 **Materials and Methods**
80 ***Mice***. 6-8-week-old Swiss Webster female mice were obtained from Charles River and allowed
81 to acclimate from travel for 1 week. Mice were housed in individually ventilated cages in a
82 pathogen-free facility with continuous food and water, with a controlled light cycle (light from
83 7am-7pm). 7-9-week-old females were estrous cycle staged using standard vaginal cytology
84 (Ajayi and Akhigbe, 2020). Mice were humanely euthanized with extended CO_2 exposure
85 followed by cervical dislocation, and female reproductive tracts were dissected. All animal
86 experiments were approved by the University of Texas at Austin Institutional Animal Care and
87 Use Committee.
88
89 ***Tissue processing & immunofluorescence***. Dissected oviducts were carefully linearized (Fig.
90 1A) by teasing apart the supercoils, gently affixing to a strip of index card to keep the tissue
91 straight, then fixing in 4% paraformaldehyde for either 4-6hr at room temperature (RT) or
92 overnight at 4°C. Linearized fixed oviducts were washed in PBS, and then incubated in 30%
93 sucrose at 4°C overnight. Following a brief incubation in NEG-50 Frozen Section Medium

94 (ThermoFisher), oviducts were embedded in NEG-50 using an ethanol/dry ice bath. 12µm frozen
95 longitudinal sections were cut on a cryostat (Leica) and dried overnight at RT. Frozen sections
96 were stored at -20°C.
97 Tissue sections were washed in PBS + 0.1% Tween20 (PBST) three times to remove
98 NEG-50. Tissues were blocked for at least 30min at RT with 5% normal donkey serum + PBS
99 (block buffer). Primary antibodies for cilia (mouse anti-acetylated tubulin, 1:1000 dilution,
100 Sigma, cat# 6-11B-1) were diluted in block buffer and incubated on slides for 2hr at RT or
101 overnight at 4°C. After washing three times with PBST, slides were incubated with Alexa-Fluor
102 coupled secondary antibodies (goat anti-mouse 647, 1:1000 dilution, ThermoFisher) and DAPI
103 (1:1000 dilution, ThermoFisher) for at least 30min at RT. After washing, slides were mounted
104 with Prolong Gold (ThermoFisher), and allowed to cure at RT in the dark overnight. Oviduct
105 sections were imaged on either a Zeiss LSM700 point scanning confocal microscope or a CSU-
106 W1 spinning disk Nikon confocal.
107
108 ***Tissue sectioning and quantitation***. Two to four sections spaced at least 100µm apart were
109 analyzed for cilia at four locations along the anteroposterior axis of the oviduct. Images from the
110 the fimbria, anterior third (approximate infundibulum), middle third (approximate ampulla), and
111 posterior third (approximate isthmus) were acquired and quantified. We quantified ciliary area as
112 previously published (Roberson et al., 2020). Briefly, we used FIJI image processing to trace the
113 lumen based on DAPI staining to approximate the luminal length. Similarly, the ciliated surface
114 of the lumen was traced and measured based on acetylated tubulin staining. From these
115 measurements, the % ciliated surface area was calculated for each image, and we plotted using
116 GraphPad Prism 8.
117
118 ***RNA isolation and cDNA synthesis.*** For 3' TagSeq (see below), dissected oviduct samples were
119 collected in duplicate for each of the four stages across both anterior and posterior regions. For
120 qPCR, samples were collected in triplicate for each estrous cycle stage across anterior, middle,
121 and posterior thirds of the mouse oviduct. Following storage in RNA*Later* Storage Solution
122 (Sigma, cat#: R0901) at -20°C, oviduct tissue was manually disrupted and the lysate was spun
123 through a QIAshredder column (Qiagen, cat#: 79656) to fully homogenize. A Qiagen RNeasy
124 mini kit (Qiagen, cat#: 74106) was used to harvest RNA for RNAseq, and the Qiagen RNeasy

125 micro kit (Qiagen, cat#: 74004) was used to harvest RNA for qPCR. Total RNA was then either
126 provided to the Genomic Sequencing and Analysis Facility at the University of Texas at Austin
127 for 3' TagSeq, or cDNA was synthesized using the iScript Reverse Transcription SuperMix
128 (BioRad, cat#: 1708841) for qPCR.
129
130 ***qPCR***. Most primers were designed from a database for mouse and human qPCR primers
131 incorporated into the UCSC genome browser (Zeisel et al., 2013). Primers for *Foxj1* and *Msx2*
132 were designed using Primer3Plus software. See Supplemental Table S-1 for primer details. We
133 confirmed specificity of primers by ensuring that they BLAST to no more than 1 site in the
134 genome. There were four outliers to this BLAST assessment: all four ribosome primer sets
135 blasted to more than 1 site in the genome, likely because there are numerous ribosomal
136 pseudogenes scattered throughout the genome (Sisu et al., 2020). In addition, we only used
137 primers whose melting curve displayed a single peak.
138 Primer sets were diluted from a stock (100µm in TE buffer) to 1µM in distilled deionized
139 H_2O. 2µL of each primer set (in technical duplicates) was allowed to dry in the bottom of a well
140 in a MicroAmp Fast Optical 96 Well Reaction Plate (Thermofisher, cat#: 43-469-06). 10µL of a
141 master mix of cDNA (250pg/well), Applied Biosystems SYBR Select Master Mix
142 (Thermofisher, cat#: 44-729-18), and distilled deionized water was added to each well, the plates
143 were sealed with MicroAmp Optical Adhesive Film (Thermofisher, cat#: 43-119-71) and
144 allowed to incubate at RT in the dark for at least 15min to rehydrate primer. Plates were run on a
145 ViiA-7 Real-Time PCR system (ThermoFisher), and CT values were auto-determined by the
146 ViiA-7 software. The standard $2^{-\Delta\Delta Ct}$ method was then used to determine fold change based on
147 the geomean of three 'housekeeping' genes (*Hprt*, *Dolk*, and *Sra1*) (Schmittgen and Livak,
148 2008).
149
150 ***TagSeq.*** Tissue samples were collected in duplicate for each of the four estrous stages across
151 both anterior and posterior regions of the mice oviduct, accounting for 16 samples in total.
152 Library preparation and sequencing for TagSeq (Lohman et al., 2016; Meyer et al., 2011), a form
153 of 3' RNA sequencing, were performed by the Genomic Sequencing and Analysis Facility
154 (GSAF) at The University of Texas at Austin. Total RNA was isolated from each sample by
155 addition of Trizol (Thermo Fisher) and the sample was transferred to a Phasemaker tube

156 (Thermo Fisher). Total RNA was extracted following the protocol supplied by the manufacturer
157 and further cleaned up using a RNeasy MinElute Cleanup Kit (Qiagen). RNA integrity number
158 (RIN) was measured using an Agilent Bioanalyzer and 100 ng of RNA was used for the TagSeq
159 protocol. The fragmentation/RT mix was prepared and added to each RNA sample, then heated
160 to 95°C for 2.5 minutes on a Thermocycler and immediately put on ice for 2 minutes. After
161 cooling and addition of the template switching oligo and SmartScribe RT, the fragmented RNA
162 reaction was incubated at 42°C for 1hr, 65°C for 15 min. Next an AmPure bead clean-up was
163 completed for the cDNA before it was amplified to incorporate the Illumina sequencing primer
164 site, followed by another cleanup. The remaining portions of the Illumina adapter (the i5 and i7
165 indices) were then added through an additional 4 cycles of PCR. Final libraries were quantified
166 with PicoGreen then pooled equally for size selection using the Blue Pippin from 355-550 bp.
167 Resulting libraries were sequenced using an Illumina HiSeq 2500 instrument (50-nt single
168 reads). Full sample dataset details are provided in Supplemental Table S-2.
169
170 ***Sequence data pre-processing.*** Fastq datasets were initially processed to collapse duplicates
171 based on TagSeq molecular barcodes (Matz). Sequencing data quality, both before and after
172 TagSeq pre-processing, was evaluated using the FastQC tool (v0.11.9) (Andrews) and reports
173 were aggregated with the MultiQC program (v1.0) (Ewels et al., 2016).
174
175 ***TagSeq data analysis.*** Single-end pseudo-alignment was performed against the mouse
176 transcriptome (GENCODE M23 transcript sequences (Frankish et al., 2019)) using kallisto
177 (v0.45.0) (Bray et al., 2016) with options -l 200 -s 50 --single-overhang –bias. Downstream
178 analysis of transcript abundance data was performed in R (v3.4.4) following protocols outlined
179 in Bioconductor (Gentleman et al., 2004). The tximport package (v1.6.0) (Soneson et al., 2015)
180 was first used to roll up transcript-level counts into gene-level counts provided to
181 the DESeq2 package (v1.18.1) (Love et al., 2014). Before further analysis, count data matrices
182 were filtered to remove genes with fewer than 1 read across all included samples. A number of
183 models were analyzed to explore the oviduct location/estrous stage relationship: Posterior versus
184 Anterior locations, first providing Early and Late data separately (n=8 each), then again
185 providing all datasets (n=16); and Late versus Early, first providing Anterior and Posterior
186 location data separately (n=8 each), then again providing all datasets (n=16). Differentially

expressed gene results reported are those with maximum adjusted p-value 0.05 and log2 fold change greater than 1.0 or less than -1.0.

Gene ontology (GO) analysis was performed using topGO R package (v2.34.0) (Alexa, 2020) with GO database org.Mm.eg.db (v3.7.0). The topGO classic algorithm and Fisher's exact test were used in count data mode. Input genes had maximum adjusted p-values of 0.10. Separate analyses were performed for up-regulated (log2 fold change 0.5 or higher) and down-regulated (log2 fold change -0.5 or lower) genes. The background gene universe consisted of observed genes used in the DESeq2 analysis.

Full DESeq2 and topGO results are provided in the supplementary zip file for GEO accession number GSE164718.

Results and Discussion

Quantification of multiciliated cell density in the cycling mouse oviduct.

Oviducts in most mammals consist of two key epithelial cell types – secretory and multiciliated cells (MCCs) – and these are unevenly distributed across the anteroposterior axis. MCCs are enriched anteriorly and secretory cells, posteriorly (Agduhr, 1927; Yamanouchi et al., 2010). While dynamic morphology changes across the estrous cycle have been described in the oviducts of many mammals (Brenner, 1969; Ferenczy et al., 1972; Novak and Everett, 1928; Shirley and Reeder, 1996; Verhage et al., 1973), the issue has not been investigated thoroughly in the mouse. To stringently assess cellular remodeling of the anteroposterior axis of the mouse oviduct across the estrous cycle, we linearized the normally supercoiled oviduct by carefully teasing apart each coil along the length of the organ (Fig. 1A), and generated longitudinal sections of linearized tissue. We then performed immunostaining for acetylated tubulin (Tub^{Ac}) to label MCC cilia, and DAPI to label nuclei (Fig. 1B-E).

By examining fimbria, anterior (approximate infundibulum), middle (approximate ampulla), and posterior (approximate isthmus) regions of the oviduct, we clearly observed the anterior bias in MCC density (Fig. 1B-E). We quantified this pattern by calculating the percentage of cilia that line the oviduct lumen, based on Tub^{Ac} staining as described previously (Roberson et al., 2020) (Fig. 1F).

By performing parallel analyses on linearized oviducts from each stage of the estrous cycle, we found that this pattern displayed no temporal changes, with the anterior oviduct being

218 significantly enriched for MCCs at all stages (Fig. 1F). The absence of significant remodeling of
219 MCCs across the estrous cycle in the mouse oviduct presents a marked contrast to other
220 mammals (Brenner, 1969; Shirley and Reeder, 1996; Verhage et al., 1973). We hypothesize that
221 this discrepancy may relate to the very short (4 to 5 day) mouse estrous cycle (Ajayi and
222 Akhigbe, 2020) and time required to eliminate and re-establish ciliated cells.
223
224 ***Determining spatiotemporal transcriptome dynamics in the mouse oviduct.***
225 Patterns of secretion, and bulk RNA and protein concentrations are known to change
226 during the mouse estrous cycle (Bronson and Hamilton, 1971). To ask if such changes have a
227 transcriptional basis, we performed 3' TagSeq, a high-throughput RNAseq profiling method that
228 captures and sequences the 3' ends of mRNA transcripts, enabling efficient estimation of relative
229 gene expression (Lohman et al., 2016; Meyer et al., 2011). We performed two biological
230 replicates of 3' TagSeq on isolated anterior (highly ciliated) and posterior (minimally ciliated)
231 oviducts at each stage of the estrous cycle (Fig. 2A). Principal component analysis (PCA)
232 revealed that the majority of expression differences occur along the AP axis (72% of variance),
233 while the estrous cycle accounts for much less variance (13%) (Fig. 2B).
234 The lack of strong variation across the estrous cycle was striking, so we considered that
235 our data might be underpowered to detect statistically significant trends across time (n=2 per
236 estrous cycle stage). We therefore repeated our analyses, collapsing the estrous cycle stages into
237 'Early' (proestrus and estrus) and 'Late' (metestrus and diestrus). This approach improved
238 differentiation between the major cycle phases; the majority of differentially expressed genes
239 (DEGs) were still found along the AP axis, not across the estrous cycle. For example, of the
240 1,758 DEGs enriched in the anterior oviduct, over 65% of them (1,158) were shared between
241 Early and Late phases (Fig. 2C). Similarly, of the 1,203 DEGs enriched in the posterior, 45%
242 (542) were shared between Early and Late (Fig 2D).
243 A more granular view of these data using volcano plots illustrates this finding. In the
244 anterior oviduct, we identified only 27 early and 14 late DEGs (Fig. 2E). Similarly, modest
245 enrichments were identified in the posterior, with 54 early and 40 late DEGs (Fig. 2F). The
246 magnitude of the expression changes was also modest, with the majority of DEG effect sizes
247 (absolute value of the log2 fold change) of two or less (59% of estrous cycle DEGs, vs. 44% of
248 AP DEGs). This result contrasts starkly to the transcriptional dynamics in the oviducts of other

249 organisms, including human, bovine, and swine, across the menstrual/estrous cycle (Bauersachs
250 et al., 2004; Cerny et al., 2015; Hess et al., 2013; Kim et al., 2018). For example, in bovine
251 anterior oviducts, 972 genes have been reported as enriched early and 597 enriched late (Cerny et
252 al., 2015), while in human anterior oviducts, 650 genes have been reported as enriched early and
253 683 enriched late (Hess et al., 2013).
254 In contrast to the muted transcriptional dynamics across the estrous cycle, we observed
255 highly robust and spatially-restricted patterns of gene expression along the AP axis of the mouse
256 oviduct. We identified 1337 genes enriched in the anterior, and 770 in the posterior early in the
257 estrous cycle (Fig. 2G). Similarly, late in the estrous cycle, 1579 genes were enriched in the
258 anterior and 975 in the posterior (Fig. 2H). Thus, our data suggest that the mouse oviduct
259 experiences relatively modest transcriptional changes as it progresses through the estrous cycle,
260 but displays robust transcriptional differences along the AP axis.
261
262 ***The mouse oviduct transcriptome is relatively stable across the estrous cycle.***
263 While our finding of modest transcriptional variation across the estrous cycle in the
264 mouse oviduct was consistent with the general lack of robust tissue remodeling, it was still
265 surprising given the impact of cycling steroid hormones on oviduct function (Barton et al.,
266 2020). To ask if the small number of DEGs we observed across time were enriched in particular
267 classes, we performed Gene Ontology (GO) analysis (Alexa, 2020) on the early versus late
268 DEGs. In the late stages, DEGs were subtly enriched for xenobiotic metabolism: xenobiotic
269 metabolic process, cellular response to xenobiotic stimulus, and xenobiotic catabolic process
270 (Supp. Fig. 1B).
271 More interestingly, DEGs in the early stages were enriched for translation-related terms:
272 peptide metabolic process, peptide biosynthetic process, translation, gene expression, and
273 cellular amide metabolic process (Supp. Fig. 1A). This enrichment for translation-related terms
274 early in the estrous cycle is consistent with the known concomitant increase in protein
275 concentration (Bronson and Hamilton, 1971). In agreement with the GO analysis, manual
276 annotation revealed an enrichment of large and small ribosome subunit genes expressed in the
277 early estrous cycle compared to late (Fig. 3A), with these genes displaying a 2 to 4-fold change
278 in abundance (Fig. 3B).

279 Further curation identified potentially interesting candidates based on their known or
280 hypothesized function in female fertility. For example, *Mki67*, *Ddit4*, *Atp1a1*, *Slc7a11*, *Mmp11*,
281 *Mmp7*, *Spock1*, and *Wsb1* were each enriched at early stages, while *Mamdc4*, *Gstp2*, *Gsta3*,
282 *Susd2*, and *Ap1g2* were enriched late, either in the anterior, posterior, or both (Fig. 3C). Among
283 these, *Mmp7* and *Slc7a11* were especially interesting, because both were upregulated early and
284 down regulated late, a pattern that is consistent with that observed in the cycling human oviduct
285 (Hess et al., 2013). *Mmp7* is part of the matrix-degrading enzyme family, and its down-
286 regulation late in the human menstrual cycle is hypothesized to help maintain oviduct matrix
287 integrity as the pre-implantation embryo travels through the organ (Hess et al., 2013). *Slc7a11* is
288 a glutamate/cysteine antiporter that is similarly regulated in the bovine oviduct (Cerny et al.,
289 2015). The majority of these DEGs also displayed modest effect sizes, similar to the ribosomal
290 genes (Fig. 3D).
291 To independently verify the observed stability of the oviduct transcriptome across the
292 estrous cycle, we performed qPCR for several of the DEGs. Consistent with the transcriptome-
293 wide data, we did not observe statistically significant changes across the estrous cycle for most
294 genes assayed (Fig. 3E-K), but the trends in expression consistently reflected trends in our
295 TagSeq data. The robust differential expression observed by qPCR between anterior and
296 posterior (see next section) indicate that these negative findings across the cycle do not reflect a
297 lack of sensitivity in our assays. Rather, we conclude that the relatively modest remodeling
298 observed in the oviduct by histology (Fig. 1) is reflected by relatively muted transcriptional
299 dynamics across the estrous cycle. While future work will be required, it seems reasonable to
300 suggest that the stability of the mouse oviduct across the estrous cycle represents an
301 evolutionarily derived state associated with the extremely rapid mouse estrous cycle, which at
302 four to five days, is much faster than in other organisms (Brenner and West, 1975).
303
304 ***The mouse oviduct displays robust transcriptional patterning along the anteroposterior axis.***
305 We next sought to understand the robust changes in gene expression we observe along
306 AP axis of the oviduct. We therefore turned again to GO Term analysis (Alexa, 2020).
307 Consistent with the strong anterior enrichment of MCCs observed by histology (Fig. 1), anterior-
308 enriched DEGs were highly enriched for cilia-related processes (Supp. Fig. 1C). In the anterior,
309 complexes that function in MCCs, including intraflagellar transport, transition zone, CPLANE,

310 and BBSome proteins (Garcia et al., 2018), as well as ciliary motility (Legendre et al., 2020) and
311 MCC transcription factors (Lewis and Stracker, 2020) were enriched (Fig. 4A). To provide
312 additional resolution to these patterns of expression for MCC-specific genes, we performed
313 qPCR for several at each estrous cycle stage, using not just anterior and posterior regions but
314 also the intervening middle region of the oviduct. We observed robust, statistically significant
315 enrichment in the anterior region for a ciliary transcription factor (*Foxj1*), a transition zone
316 complex gene (*Tmem231*), two ciliogenesis genes (*Ift140* and *Ift57*), and one gene encoding a
317 component of the ciliary beating machinery (*Dnah9*) (Fig. 4F-I).
318 To investigate whether mouse anterior oviduct DEGs are similar to human multiciliated
319 tissues, we compared our MCC-enriched dataset to the recently published human multiciliated
320 tissue transcriptional signature (Patir et al., 2020). The analysis of four human multiciliated
321 tissues, including ependymal, oviduct, trachea, and sperm, identified 248 genes expressed by all
322 four tissues. Of those, we find 166 of them to be differentially expressed in the anterior of the
323 mouse oviduct (data not shown), suggesting that, transcriptionally, multiciliated genes of the
324 mouse oviduct are highly similar to those of human multiciliated tissues.
325 Non-ciliated epithelial cells in the posterior oviduct consist predominantly of secretory
326 cells (Agduhr, 1927; Ghosh et al., 2017). Accordingly, our posterior-enriched gene set was
327 strongly enriched for transport and secretion GO Terms (Supp. Fig. 4), including solute carriers,
328 transport ATPases, Ca^{2+} and K^{+} channels (Fig. 4A). These GO terms are similar to previously
329 published datasets from other mammals, including cows and humans, where vesicle-mediated
330 transport, endocytosis, and exocytosis were among the main processes enriched in the posterior
331 (Gonella-Diaza et al., 2017; Maillo et al., 2016; Rose et al., 2020). We confirmed this trend using
332 qPCR for a transport ATPase (*Atp1b1*) and a solute carrier (*Slc39a8*); both were significantly
333 enriched in the posterior (Fig. 4K, L).
334 Interestingly, certain genes enriched in the mouse oviduct posterior are differentially
335 expressed across the human menstrual cycle (Hess et al., 2013). For example, of the 33 solute
336 carrier (Slc) genes that are enriched in the posterior of the mouse oviduct, eight of them are also
337 differentially expressed across the human menstrual cycle, including *Slc2a3*, *Slc22a23*, *Slc27a3*,
338 *Slc39a14*, *Slc39a2*, *Slc39a8*, *Slc4A7*, *Slc8a1* (Hess et al., 2013). These Slc genes are
339 hypothesized to be important for secreting amino acids and other nutrients into the oviductal
340 lumen to aid in preimplantation embryonic development. Further studies investigating SLC

341 expression dynamics across both humans and mice may offer insights into the evolution of
342 mammalian reproduction and divergence underlying these secretory cell types.
343
344 ***Patterned expression of known developmental signaling systems along the anteroposterior***
345 ***axis of the adult oviduct.***
346 Our analysis of anteroposterior gene expression patterns also revealed several previously
347 unreported trends. First, the genes up-regulated specifically in the posterior oviduct were
348 strongly enriched for GO Terms related to embryonic development (Supp. Fig. 1D). For
349 example, all three non-canonical Wnt ligands, *Wnt5a*, *Wnt7a*, and *Wnt11* were enriched in the
350 posterior region of the oviduct (Fig. 4B, N, O). Moreover, two antagonists of canonical Wnt
351 signaling were also differentially expressed, but in a curious fashion: *Dkk2* was enriched in the
352 posterior, while *Dkk3* was enriched in the anterior (Fig. 4B). Components of the FGF signaling
353 pathway were also differentially expressed: *Fgf1*, *Fgf16*, and *Fgf2* were enriched in the posterior,
354 while only the FGF receptor, *Fgfr3*, was enriched in the anterior (Fig. 4C). Finally, multiple
355 transcription factors were differentially expressed, including Msx2 (Fig. 4M) and several Hox
356 genes, including *Hoxa9* and *Hoxa10* (Fig. 4D), both of which are involved in female
357 reproductive tract development (Du and Taylor, 2015). Other differentially expressed Hox genes
358 include *Hoxb2*, *Hoxb7*, *Hoxb8*, and *Hoxc10* (Fig. 4D). We confirmed the differential expression
359 of many of the developmental regulators using qPCR (Fig. 4M-O)
360 Not all signaling pathways displayed patterned expression, and an excellent example is
361 the Planar Cell Polarity (PCP) pathway (Fig. 4E). The PCP system is essential for normal
362 polarized ciliary beating in the oviduct, so most PCP genes are expressed in the oviduct (Koyama
363 et al., 2019; Shi et al., 2014). Strikingly however, none displayed enrichment along the AP axis
364 (Fig. 4E).
365 In contrast to intracellular effectors of PCP signaling, expression of non-canonical Wnt
366 ligands was strongly polarized, which was of interest for multiple reasons. First, Wnt signaling is
367 necessary to maintain stemness in human oviduct organoid cultures (Kessler et al., 2015), and
368 secretory cells are thought to be the progenitors of MCCs in the mouse oviduct. Thus, it may be
369 that posteriorly enriched Wnt signaling maintains the progenitor capabilities of posteriorly
370 enriched secretory cells (Ghosh et al., 2017). Second, *Wnt5a*/*7a*/*11* are known to orient PCP
371 signaling, providing directional cues for the apical surface of cells and driving coordinated

372 ciliary beating in multiciliated tissues (Butler and Wallingford, 2017; Gao et al., 2011; Koyama
373 et al., 2019; Ossipova et al., 2015). While the oviduct is planar polarized – i.e. Vangl2 localizes
374 anteriorly in oviduct epithelial cells – it is unknown where the directional cue originates (Shi et
375 al., 2016). Our data raise the possibility that posteriorly enriched *Wnt5a/7a/11* orients Vangl2
376 localization to the anterior side of the oviduct epithelium, thereby regulating ciliary flow towards
377 the posterior oviduct. Our experiments also indicate that PCP signaling components are evenly
378 expressed across the AP axis of the oviduct, While the impact of planar polarization on MCCs is
379 fairly well studied, the corresponding impact on secretory cells remains unknown.
380

381 **Conclusions**

382 In summary, our transcriptome profiling data fills a major gap in mouse oviduct investigations.
383 While confirming reports made using other methods, our detailed anteroposterior axis and
384 estrous stage analyses reveal novel gene expression patterns as well as providing a foundation for
385 further studies. Hypotheses generated from these data can inform additional explorations using
386 orthogonal methods such as single-cell sequencing and proteomics. Such studies have the
387 potential to identify specific cell types associated with expression trends observed here, as well
388 as quantifying actual cellular protein abundances which may differ from RNA expression.
389

390 **Acknowledgements**

391 We thank the Genome Sequencing and Analysis facility at the University of Texas at Austin for
392 their support and assistance with sequencing. This research was supported by funding from the
393 National Institutes of Health (F32HD095618 to E.C.R., R01HL117164 to J.B.W.,
394 R01HD085901 to J.B.W. and E.M.M., and R35GM122480 to E.M.M.), the American Heart
395 Association predoctoral fellowship (#18PRE34060258) to R.K.G., and the Welch Foundation (F-
396 1515, to E.M.M.).
397
398
399
400
401

402 **Figure 1. The mouse oviduct displays anteroposterior patterning that does not change**
403 **across the estrous cycle.** A) A linearized mouse oviduct, where the anterior is close to the ovary
404 and the posterior is close to the uterus. The insert shows a non-linearized supercoiled mouse
405 oviduct (insert, arrow). Oviducts were collected at B) proestrus, C) estrus, D) metestrus, and E)
406 diestrus, linearized, and imaged for nuclei (DAPI, magenta) and cilia (Tub^{Ac}, green) along the
407 AP axis (fimbria, anterior, middle, and posterior). Scale bar = 100µm. F) Quantitation of the
408 percent ciliated surface area along the oviduct lumen in each of the four estrous stages. Some
409 error bars are too small to be seen. * = p< 0.05.

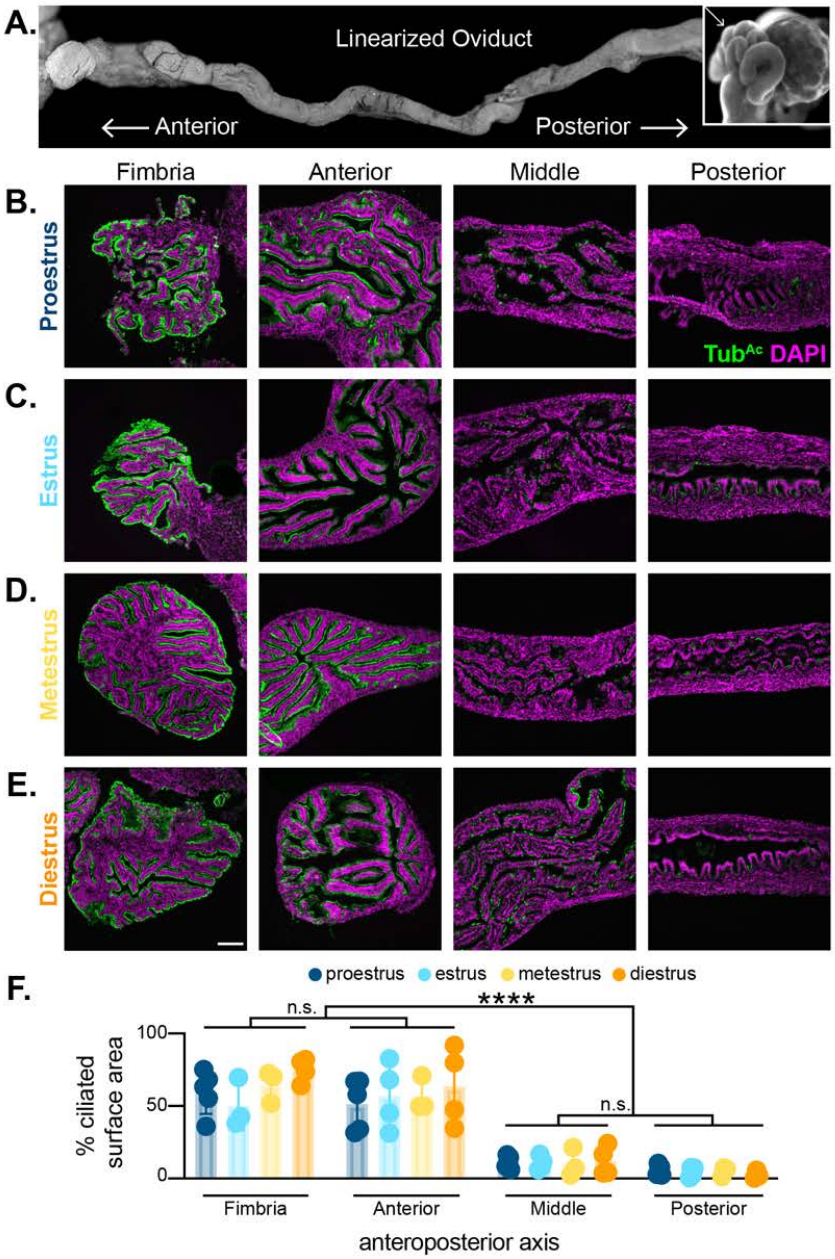

432 **Figure 2. RNAseq of the oviduct shows major differences along the anteroposterior axis**
433 **and minor change across the estrous cycle**. A) Oviducts were dissected and linearized from
434 each stage of the estrous cycle (n=2 each stage). RNA from the anterior and posterior thirds of
435 each oviduct was collected and submitted for 3' TagSeq. B) Principal Component Analysis
436 (PCA) of the sixteen 3'TagSeq datasets. AP location (displayed as symbols) accounts for most of
437 the variance while estrous cycle stage (displayed as colors) accounts for a lesser part with good
438 separation between early (Proestrus, Estrus) and late (Metestrus, Diestrus) phases. C) Overlap
439 between the anterior DEGs at early and late estrous cycle phases. D) Overlap between the
440 posterior DEGs at early and late phases of the estrous cycle. Volcano plots of oviduct E) anterior
441 and F) posterior compare early and late DEGs. Volcano plots of estrous cycle G) early and H)
442 late phases cycle show anterior and posterior DEGs. Red points are genes significant at both
443 adjusted P-value (<= 0.05) and effect size (log2 fold change <= -1 or >= 1).

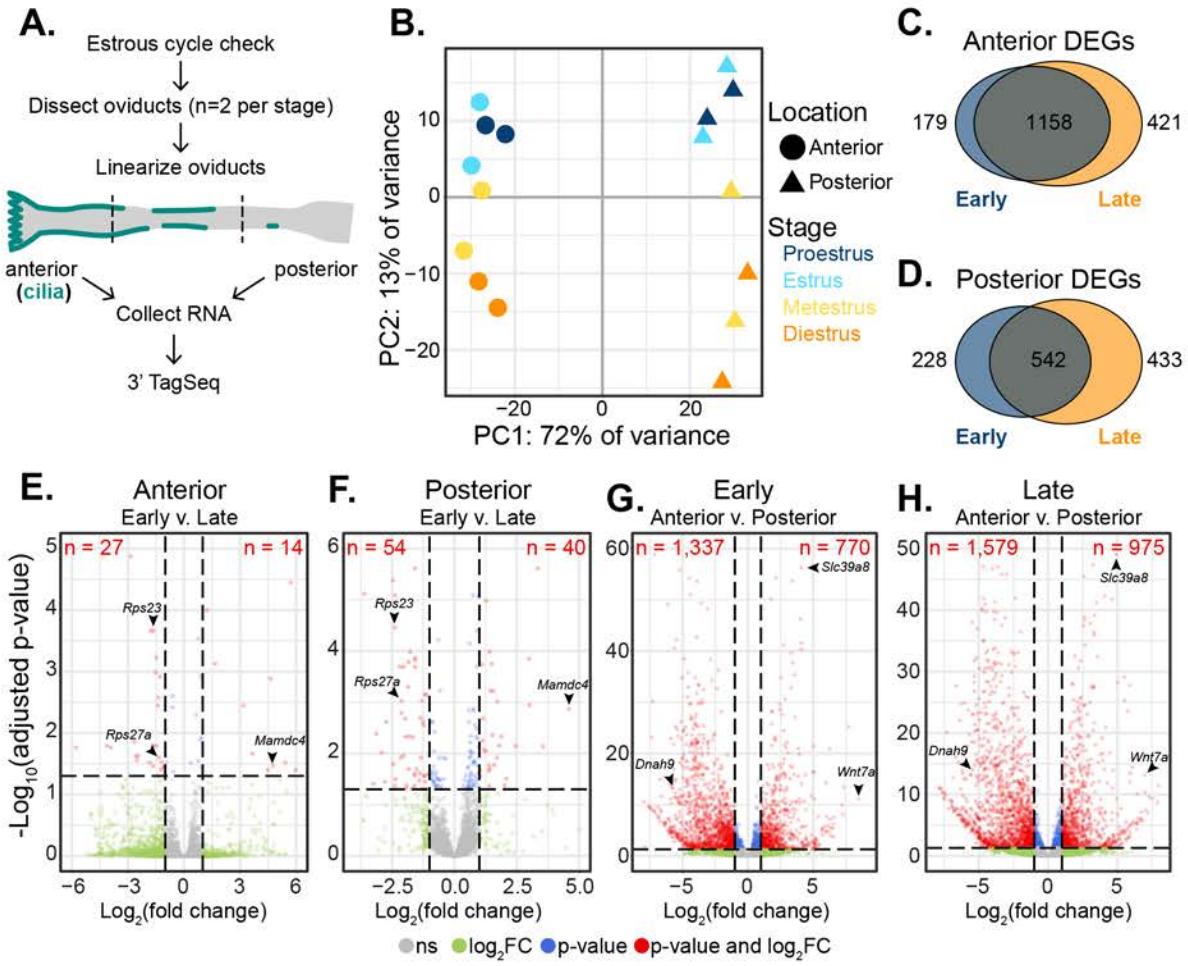

444
445

Figure 3. The mouse oviduct transcriptome is remarkably stable across the estrous cycle. A) Heatmap depicting expression of ribosomal genes across the estrous cycle where rows indicate genes and columns indicate the estrous cycle stage (P- proestrus, E- estrus, M- metestrus, D- diestrus). B) The effect size (absolute value of the log2 fold change) of the ribosomal genes was generally modest (under 2). C) Heatmap of other DEGs. D) These genes also generally have modest but consistent effect sizes. E-K) qPCR histograms of select genes from B and D along the anteroposterior axis at each estrous cycle stage. All heatmap scales use DESeq2 variance stabilized counts.

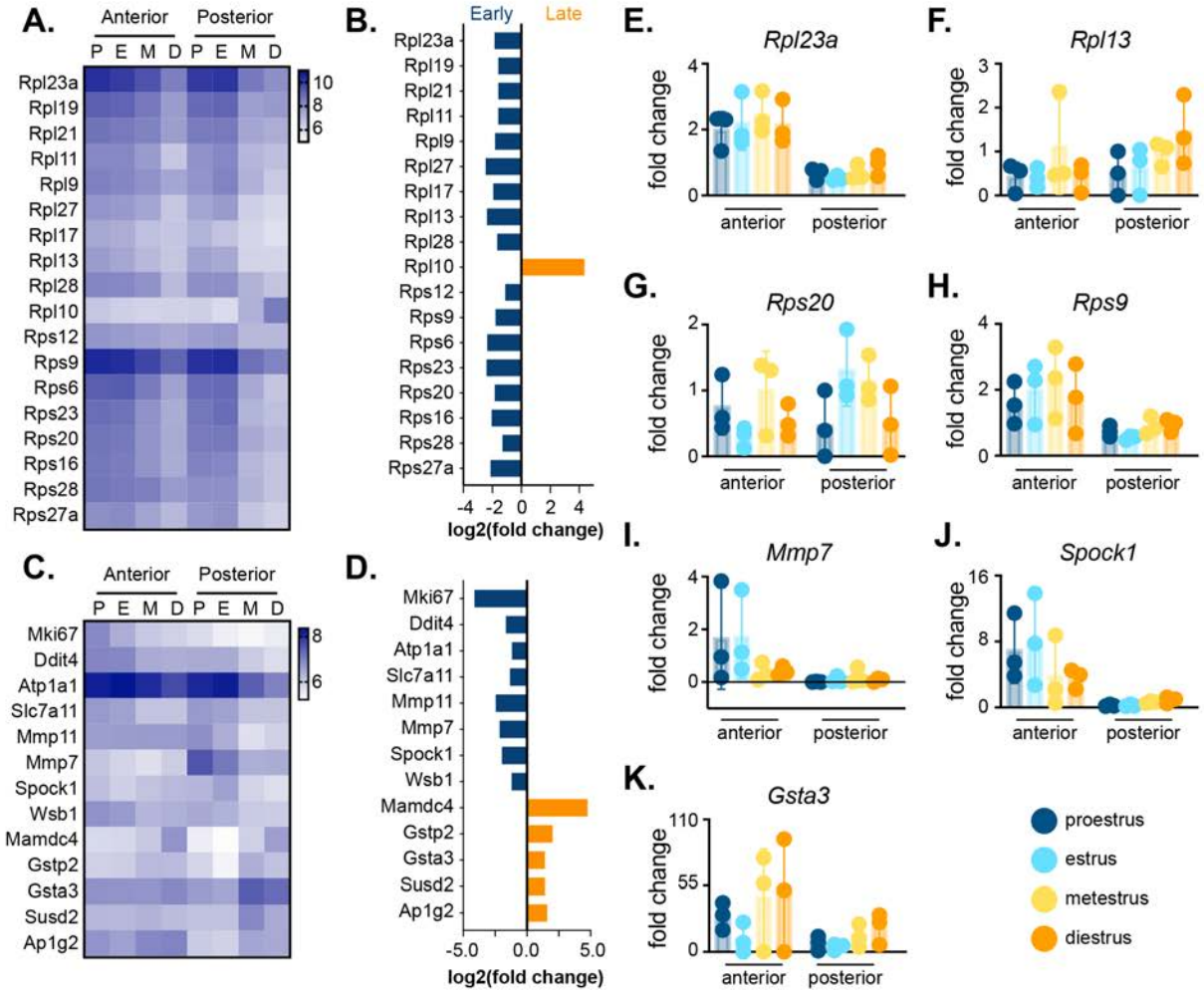

Figure 4. The mouse oviduct displays robust transcriptional patterning along the anteroposterior axis. A) Heatmap showing expression dynamics of DEGs across the anterior and posterior, including cilia-related genes and complexes, solute carriers, transport ATPases, and calcium and potassium channels. Additional heatmaps of genes in developmental signaling pathways, including B) Wnt signaling, C) FGF signaling, D) Hox genes, and E) PCP signaling. F-R) qPCR histograms of select genes from A-E along the anteroposterior axis at each estrous cycle stage: anterior-enriched genes *Foxj1*, *Tmem231*, *Ift140*, *Ift57*, *Dnah9;* posterior-enriched genes *Atp1b1*, *Slc29a8*, *Msx2*, *Wnt7a*, *Wnt5a*; and other qPCR assayed genes *Prickle1*, *Vangl2*, *Pax8*.

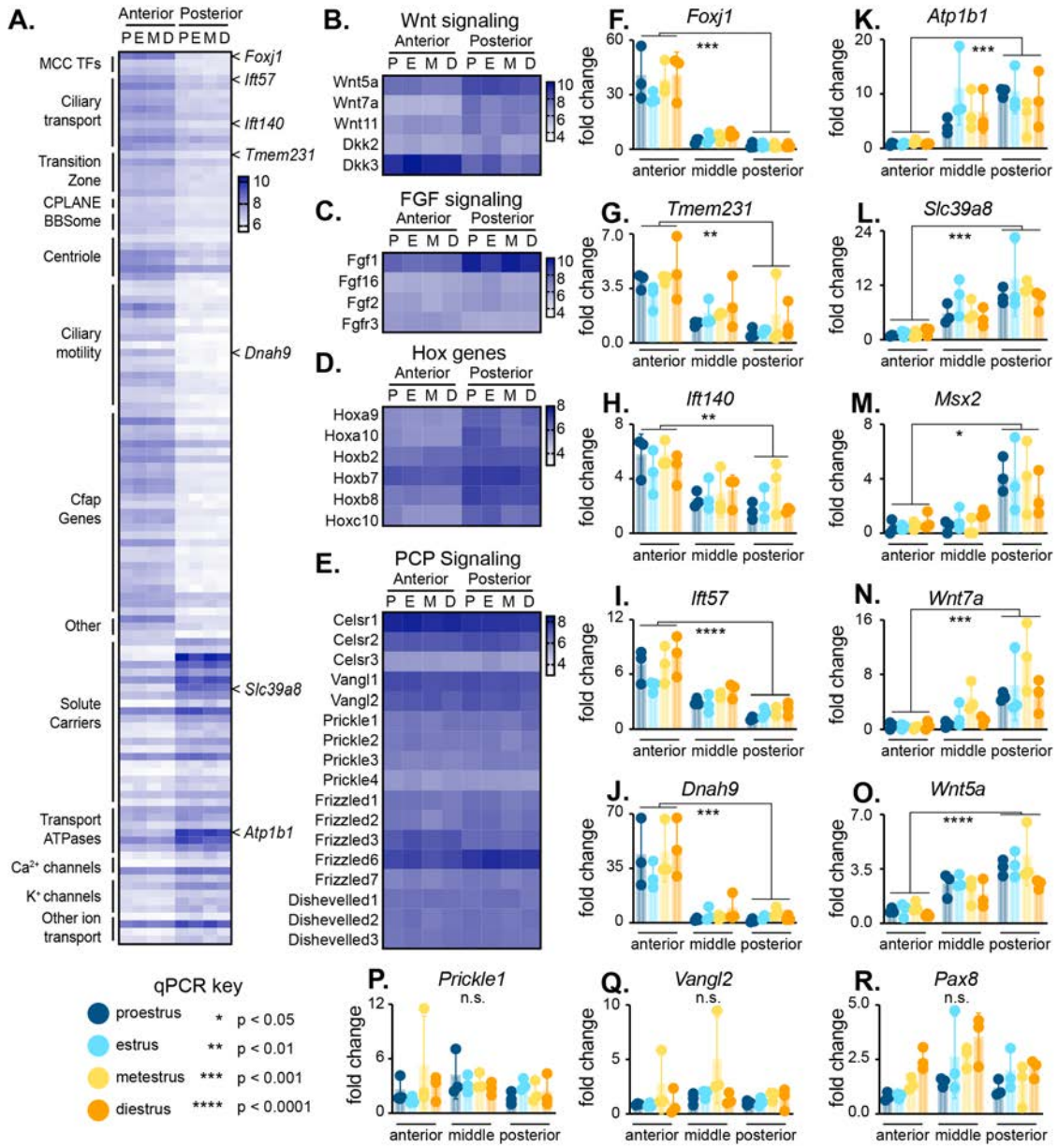

471 **Supplementary Figure 1. Significant GO terms associated with oviduct transcriptome**
472 **analysis.** Histograms depicting significant GO terms for A) early, B) late, C) anterior, and D)
473 posterior DEGs.

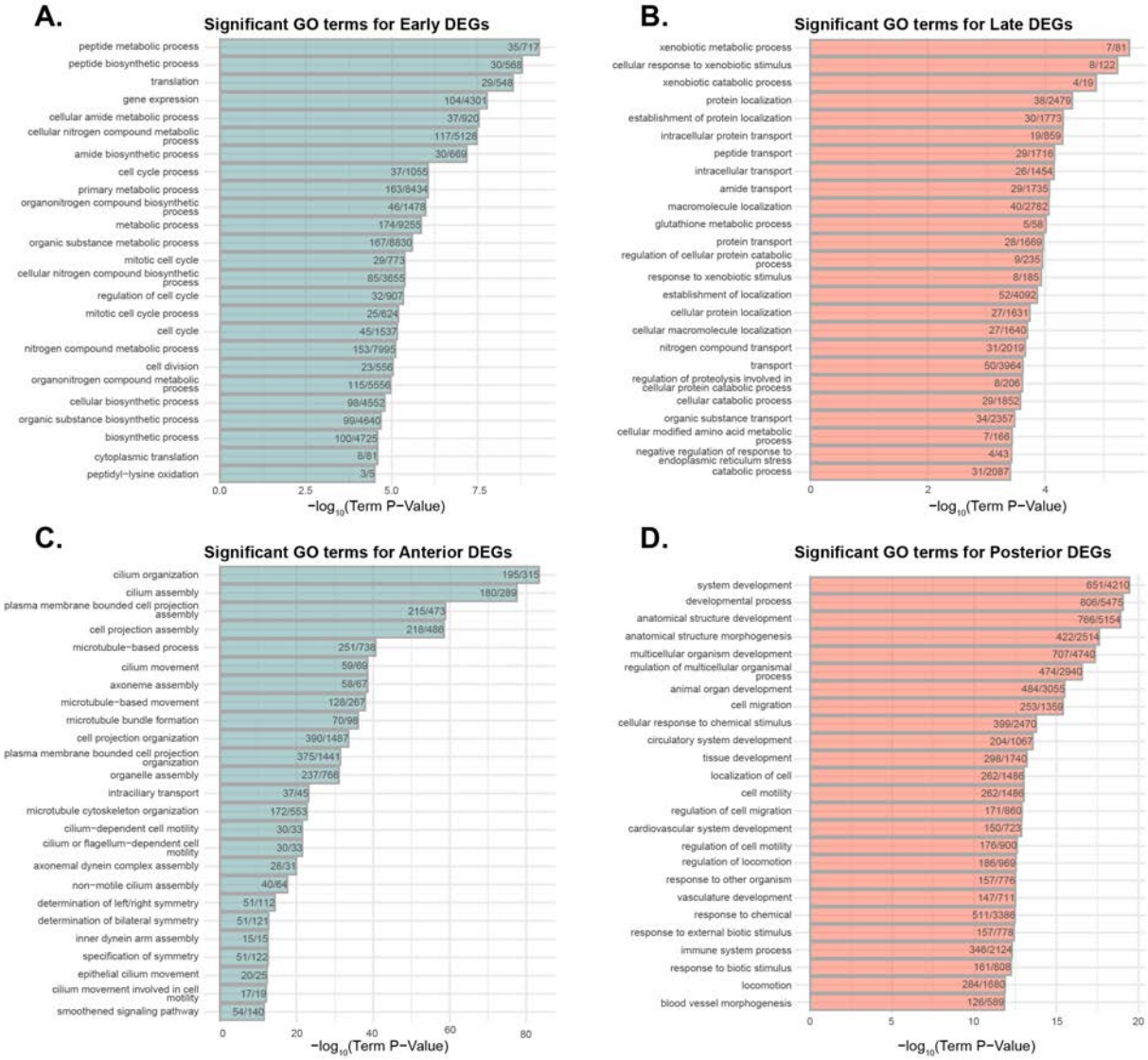

474
475
476 **Supplemental spreadsheet tabs:**
477 **S-1. Primers used for qPCR.**
478 **S-2. Description of the sample datasets used.**
479 Full DEG and GO term details are available in the Supplementary zip file for GEO accession
480 number GSE164718.
481

482 **References**

483 Agduhr, E., 1927. Studies on the structure and development of the bursa ovarica and the tuba
484 uterina in the Mouse. Acta Zoologica Stockholm 8, pp. 1-133.

485 Ajayi, A.F., Akhigbe, R.E., 2020. Staging of the estrous cycle and induction of estrus in
486 experimental rodents: an update. Fertil Res Pract 6, 5.

487 Alexa, A., Rahnenfuhrer, J, 2020. topGO: Enrichment Analysis for Gene Ontology, R package
488 version 2.40.0.

489 Andrews, S., FastQC. Babraham Bioinformatics, p.
490 https://www.bioinformatics.babraham.ac.uk/projects/fastqc/.

491 Barton, B.E., Herrera, G.G., Anamthathmakula, P., Rock, J.K., Willie, A., Harris, E.A.,
492 Takemaru, K.I., Winuthayanon, W., 2020. Roles of steroid hormones in oviductal function.
493 Reproduction 159, R125-r137.

494 Bauersachs, S., Rehfeld, S., Ulbrich, S.E., Mallok, S., Prelle, K., Wenigerkind, H., Einspanier,
495 R., Blum, H., Wolf, E., 2004. Monitoring gene expression changes in bovine oviduct epithelial
496 cells during the oestrous cycle. J Mol Endocrinol 32, 449-466.

497 Bray, N.L., Pimentel, H., Melsted, P., Pachter, L., 2016. Near-optimal probabilistic RNA-seq
498 quantification. Nat Biotechnol 34, 525-527.

499 Brenner, R.M., 1969. Renewal of oviduct cilia during the menstrual cycle of the rhesus monkey.
500 Fertil Steril 20, 599-611.

501 Brenner, R.M., West, N.B., 1975. Hormonal regulation of the reproductive tract in female
502 mammals. Annu Rev Physiol 37, 273-302.

503 Bronson, F.H., Hamilton, T.H., 1971. Concentrations of nucleic acids and protein in the mouse
504 oviduct during the oestrous cycle and after steroid replacement. J Reprod Fertil 25, 283-286.

505 Butler, M.T., Wallingford, J.B., 2017. Planar cell polarity in development and disease. Nat Rev
506 Mol Cell Biol 18, 375-388.

507 Bylander, A., Nutu, M., Wellander, R., Goksör, M., Billig, H., Larsson, D.G., 2010. Rapid
508 effects of progesterone on ciliary beat frequency in the mouse fallopian tube. Reprod Biol
509 Endocrinol 8, 48.

510 Cerny, K.L., Garrett, E., Walton, A.J., Anderson, L.H., Bridges, P.J., 2015. A transcriptomal
511 analysis of bovine oviductal epithelial cells collected during the follicular phase versus the luteal
512 phase of the estrous cycle. Reprod Biol Endocrinol 13, 84.

513 Coy, P., Garcia-Vazquez, F.A., Visconti, P.E., Aviles, M., 2012. Roles of the oviduct in
514 mammalian fertilization. Reproduction 144, 649-660.

515 Coy, P., Yanagimachi, R., 2015. The Common and Species-Specific Roles of Oviductal Proteins
516 in Mammalian Fertilization and Embryo Development. BioScience 65, 973-984.

517 Du, H., Taylor, H.S., 2015. The Role of Hox Genes in Female Reproductive Tract Development,
518 Adult Function, and Fertility. Cold Spring Harb Perspect Med 6, a023002.

519 Ewels, P., Magnusson, M., Lundin, S., Kaller, M., 2016. MultiQC: summarize analysis results
520 for multiple tools and samples in a single report. Bioinformatics 32, 3047-3048.

521 Ferenczy, A., Richart, R.M., Agate, F.J., Jr., Purkerson, M.L., Dempsey, E.W., 1972. Scanning
522 electron microscopy of the human fallopian tube. Science 175, 783-784.

523 Frankish, A., Diekhans, M., Ferreira, A.M., Johnson, R., Jungreis, I., Loveland, J., Mudge, J.M.,
524 Sisu, C., Wright, J., Armstrong, J., Barnes, I., Berry, A., Bignell, A., Carbonell Sala, S., Chrast,
525 J., Cunningham, F., Di Domenico, T., Donaldson, S., Fiddes, I.T., Garcia Giron, C., Gonzalez,
526 J.M., Grego, T., Hardy, M., Hourlier, T., Hunt, T., Izuogu, O.G., Lagarde, J., Martin, F.J.,
527 Martinez, L., Mohanan, S., Muir, P., Navarro, F.C.P., Parker, A., Pei, B., Pozo, F., Ruffier, M.,
528 Schmitt, B.M., Stapleton, E., Suner, M.M., Sycheva, I., Uszczynska-Ratajczak, B., Xu, J., Yates,
529 A., Zerbino, D., Zhang, Y., Aken, B., Choudhary, J.S., Gerstein, M., Guigo, R., Hubbard, T.J.P.,
530 Kellis, M., Paten, B., Reymond, A., Tress, M.L., Flicek, P., 2019. GENCODE reference
531 annotation for the human and mouse genomes. Nucleic Acids Res 47, D766-D773.

532 Gao, B., Song, H., Bishop, K., Elliot, G., Garrett, L., English, M.A., Andre, P., Robinson, J.,
533 Sood, R., Minami, Y., Economides, A.N., Yang, Y., 2011. Wnt signaling gradients establish

534 planar cell polarity by inducing Vangl2 phosphorylation through Ror2. Developmental cell 20,
535 163-176.

536 Garcia, G., 3rd, Raleigh, D.R., Reiter, J.F., 2018. How the Ciliary Membrane Is Organized
537 Inside-Out to Communicate Outside-In. Curr Biol 28, R421-R434.

538 Gentleman, R.C., Carey, V.J., Bates, D.M., Bolstad, B., Dettling, M., Dudoit, S., Ellis, B.,
539 Gautier, L., Ge, Y., Gentry, J., Hornik, K., Hothorn, T., Huber, W., Iacus, S., Irizarry, R., Leisch,
540 F., Li, C., Maechler, M., Rossini, A.J., Sawitzki, G., Smith, C., Smyth, G., Tierney, L., Yang,
541 J.Y., Zhang, J., 2004. Bioconductor: open software development for computational biology and
542 bioinformatics. Genome Biol 5, R80.

543 Ghosh, A., Syed, S.M., Tanwar, P.S., 2017. In vivo genetic cell lineage tracing reveals that
544 oviductal secretory cells self-renew and give rise to ciliated cells. Development (Cambridge,
545 England) 144, 3031-3041.

546 Gonella-Diaza, A.M., da Silva Andrade, S.C., Sponchiado, M., Pugliesi, G., Mesquita, F.S., Van
547 Hoeck, V., de Francisco Strefezzi, R., Gasparin, G.R., Coutinho, L.L., Binelli, M., 2017.
548 Oviductal transcriptional profiling of a bovine fertility model by next-generation sequencing.
549 Genom Data 13, 27-29.

550 Herrera, G.G.B., Lierz, S.L., Harris, E.A., Donoghue, L.J., Hewitt, S.C., Rodriguez, K.F.,
551 Jefferson, W.N., Lydon, J.P., DeMayo, F.J., Williams, C.J., Korach, K.S., Winuthayanon, W.,
552 2020. Oviductal Retention of Embryos in Female Mice Lacking Estrogen Receptor α in the
553 Isthmus and the Uterus. Endocrinology 161.

554 Hess, A.P., Talbi, S., Hamilton, A.E., Baston-Buest, D.M., Nyegaard, M., Irwin, J.C., Barragan,
555 F., Kruessel, J.S., Germeyer, A., Giudice, L.C., 2013. The human oviduct transcriptome reveals
556 an anti-inflammatory, anti-angiogenic, secretory and matrix-stable environment during embryo
557 transit. Reprod Biomed Online 27, 423-435.

558 Kessler, M., Hoffmann, K., Brinkmann, V., Thieck, O., Jackisch, S., Toelle, B., Berger, H.,
559 Mollenkopf, H.J., Mangler, M., Sehouli, J., Fotopoulou, C., Meyer, T.F., 2015. The Notch and

560 Wnt pathways regulate stemness and differentiation in human fallopian tube organoids. Nat
561 Commun 6, 8989.

562 Kim, J.M., Park, J.E., Yoo, I., Han, J., Kim, N., Lim, W.J., Cho, E.S., Choi, B., Choi, S., Kim,
563 T.H., Te Pas, M.F.W., Ka, H., Lee, K.T., 2018. Integrated transcriptomes throughout swine
564 oestrous cycle reveal dynamic changes in reproductive tissues interacting networks. Sci Rep 8,
565 5436.

566 Koyama, H., Shi, D., Fujimori, T., 2019. Biophysics in oviduct: Planar cell polarity, cilia,
567 epithelial fold and tube morphogenesis, egg dynamics. Biophys Physicobiol 16, 89-107.

568 Legendre, M., Zaragosi, L.E., Mitchison, H.M., 2020. Motile cilia and airway disease. Semin
569 Cell Dev Biol.

570 Lewis, M., Stracker, T.H., 2020. Transcriptional regulation of multiciliated cell differentiation.
571 Semin Cell Dev Biol.

572 Lohman, B.K., Weber, J.N., Bolnick, D.I., 2016. Evaluation of TagSeq, a reliable low-cost
573 alternative for RNAseq. Mol Ecol Resour 16, 1315-1321.

574 Love, M.I., Huber, W., Anders, S., 2014. Moderated estimation of fold change and dispersion for
575 RNA-seq data with DESeq2. Genome Biol 15, 550.

576 Maillo, V., de Frutos, C., O'Gaora, P., Forde, N., Burns, G.W., Spencer, T.E., Gutierrez-Adan,
577 A., Lonergan, P., Rizos, D., 2016. Spatial differences in gene expression in the bovine oviduct.
578 Reproduction 152, 37-46.

579 Matz, M., Tag-based RNAseq, pp. https://github.com/z0on/tag-based_RNAseq.

580 Meyer, E., Aglyamova, G.V., Matz, M.V., 2011. Profiling gene expression responses of coral
581 larvae (Acropora millepora) to elevated temperature and settlement inducers using a novel RNA-
582 Seq procedure. Mol Ecol 20, 3599-3616.

583 Novak, E., Everett, H., 1928. Cyclical and other variations in the tubal epithelium. American
584 Journal of Obstetrics and Gynecology 16, 499-530.

585 Ossipova, O., Kim, K., Sokol, S.Y., 2015. Planar polarization of Vangl2 in the vertebrate neural
586 plate is controlled by Wnt and Myosin II signaling. Biol Open 4, 722-730.

587 Patir, A., Fraser, A.M., Barnett, M.W., McTeir, L., Rainger, J., Davey, M.G., Freeman, T.C.,
588 2020. The transcriptional signature associated with human motile cilia. Scientific Reports 10,
589 10814.

590 Roberson, E.C., Tran, N.K., Konjikusic, M.J., Fitch, R.D., Gray, R.S., Wallingford, J.B., 2020. A
591 comparative study of the turnover of multiciliated cells in the mouse trachea, oviduct, and brain.
592 Dev Dyn 249, 898-905.

593 Rose, I.M., Bidarimath, M., Webster, A., Godwin, A.K., Flesken-Nikitin, A., Nikitin, A.Y.,
594 2020. WNT and inflammatory signaling distinguish human Fallopian tube epithelial cell
595 populations. Sci Rep 10, 9837.

596 Schmittgen, T.D., Livak, K.J., 2008. Analyzing real-time PCR data by the comparative C(T)
597 method. Nature protocols 3, 1101-1108.

598 Shi, D., Komatsu, K., Hirao, M., Toyooka, Y., Koyama, H., Tissir, F., Goffinet, A.M., Uemura,
599 T., Fujimori, T., 2014. Celsr1 is required for the generation of polarity at multiple levels of the
600 mouse oviduct. Development (Cambridge, England) 141, 4558-4568.

601 Shi, D., Komatsu, K., Uemura, T., Fujimori, T., 2011. Analysis of ciliary beat frequency and
602 ovum transport ability in the mouse oviduct. Genes Cells 16, 282-290.

603 Shi, D., Usami, F., Komatsu, K., Oka, S., Abe, T., Uemura, T., Fujimori, T., 2016. Dynamics of
604 planar cell polarity protein Vangl2 in the mouse oviduct epithelium. Mech Dev 141, 78-89.

605 Shirley, B., Reeder, R.L., 1996. Cyclic changes in the ampulla of the rat oviduct. J Exp Zool 276,
606 164-173.

607 Sisu, C., Muir, P., Frankish, A., Fiddes, I., Diekhans, M., Thybert, D., Odom, D.T., Flicek, P.,
608 Keane, T.M., Hubbard, T., Harrow, J., Gerstein, M., 2020. Transcriptional activity and strain-
609 specific history of mouse pseudogenes. Nat Commun 11, 3695.

610 Soneson, C., Love, M.I., Robinson, M.D., 2015. Differential analyses for RNA-seq: transcript-
611 level estimates improve gene-level inferences. F1000Res 4, 1521.

612 Sowamber, R., Nelson, O., Dodds, L., DeCastro, V., Paudel, I., Milea, A., Considine, M., Cope,
613 L., Pinto, A., Schlumbrecht, M., Slomovitz, B., Shaw, P.A., George, S.H.L., 2020. Integrative
614 Transcriptome Analyses of the Human Fallopian Tube: Fimbria and Ampulla-Site of Origin of
615 Serous Carcinoma of the Ovary. Cancers (Basel) 12.

616 Stewart, C.A., Behringer, R.R., 2012. Mouse oviduct development. Results Probl Cell Differ 55,
617 247-262.

618 Suarez, S.S., 2016. Mammalian sperm interactions with the female reproductive tract. Cell
619 Tissue Res 363, 185-194.

620 Talbot, P., Geiske, C., Knoll, M., 1999. Oocyte pickup by the mammalian oviduct. Mol Biol Cell
621 10, 5-8.

622 Verhage, H., Abel Jr, J., Tietz Jr, W., Barrau, M., 1973. Development and maintenance of the
623 oviductal epithelium during the estrous cycle in the bitch. Biology of reproduction 9, 460-474.

624 Winuthayanon, W., Bernhardt, M.L., Padilla-Banks, E., Myers, P.H., Edin, M.L., Lih, F.B.,
625 Hewitt, S.C., Korach, K.S., Williams, C.J., 2015. Oviductal estrogen receptor alpha signaling
626 prevents protease-mediated embryo death. Elife 4, e10453.

627 Yamanouchi, H., Umezu, T., Tomooka, Y., 2010. Reconstruction of oviduct and demonstration
628 of epithelial fate determination in mice. Biology of reproduction 82, 528-533.

629 Zeisel, A., Yitzhaky, A., Bossel Ben-Moshe, N., Domany, E., 2013. An accessible database for
630 mouse and human whole transcriptome qPCR primers. Bioinformatics 29, 1355-1356.
631
632

Table S-1

Gene	Sequence
Rpl23a	F: 5' - AGGCAGCCAAAATATCCTCG - 3'
	R: 5' - TTCTTCATGGCTGACTCCGT - 3'
Rps9	F: 5' - GCTAGACGAGAAGGATCCCC – 3'
	R: 5' - ATCCAGCTTCATCTTGCCCT – 3
Rpl13	F: 5' - TACTGAAGCCCCACTTCCAC - 3'
	R: 5' - CGGACCTTGGTGTGGTATCT - 3'
Rps20	F: 5' - GAACAAGTCGGTCAGGAAGC - 3'
	R: 5' - CTCTGATCAAGTCCGCACAA - 3'
Mmp7	F: 5' - CCTAGGCGGAGATGCTCACT -3'
	R: 5' - GAGAGTGGCCAAATTCATGG - 3'
Spock1	F: 5'- CTGAAGCCCAAAGCAGAGAA - 3'
	R: 5' - CTCATGAAGAGCCCCGAAC - 3'
Gsta3	F: 5' - GATTTAGACTCCAAGCGGCA - 3'
	R: 5' - TTCCCCTGCCATCAAAGTAA - 3'
Foxj1	F: 5'- TGTGGATCTTACAGTCCATGGC -3'
	R: 5'- TCTCATCAAAGTCCAGGCTGTC -3'
Tmem231	F: 5'- AACAGAAGCAGCCACTGAGC -3'
	R: 5'- AACAATGTGGGTGAGGTCGT -3'
Ift140	F: 5'- ATTCCTGGCAGTCGCATCTA -3'
	R: 5'- GAAGTGGCCTGGAAAGACCT -3'
Ift57	F: 5'- GCGGAATGGAGCCTAGAAGT -3'
	R: 5'- CTTTTGTGCTGGTGCATTTG -3'
Dnah9	F: 5'- TGTGAACGCATGAACATCCT -3'
	R: 5'- TTCCATCTCACTGGTCATGGT -3'
Msx2	F: 5'- AGCTGAAAATGGCTGCCAAG -3'
	R: 5'- TAGGATGCGCCGTATATGGATG -3'
Wnt7a	F: 5'- GCCTGGACGAGTGTCAGTTT -3'
	R: 5'- AATCGCATAGGTGAAGGCAG -3'
Wnt5a	F: 5'- CACGTTTTTCTCCTTCGCC -3'
	R: 5'- AGTTGGCTGCAGAGAGGCT -3'
Slc39a8	F: 5'- GGCCAGCTGCACTTCAAC -3'
	R: 5'- GCAGATGGCAGAGAAGTTCG -3'
Atp1b1	F: 5'- GAAGCCCTGCATCATTATCAA -3'
	R: 5'- GAACAGGCAGGACATTTGGA -3'
Prickle1	F: 5'- GTGGCTGCTTCGAGTCTCTC -3'
	R: 5'- TCGTAGGTCATCTGTGCGTG -3'
Vangl2	F: 5'- TACTACGAGGAAGCCGAGCA -3'
	R: 5'- CTTCCTGCAGCCGCTTAAT -3'
Pax8	F: 5' – ACAGGGCAGCTATGCCTCTT - 3'
	R: 5' – GCTGTAGGCATTGCCAGAAT - 3'
Hprt	F: 5' – CATAACCTGGTTCATCATCGC - 3'
	R: 5' – TCCTCCTCAGACCGCTTTT - 3'
Dolk	F: 5' – CAGTGTGGGACCGATACTCCT - 3'
	R: 5' – CCAAGCAAAGGCATGACCA - 3'
Sra1	F: 5' – ACGACCCGCCACAATTCTC - 3'
	R: 5' – CTGGAAGCCTTACTTGAAGGAG - 3'

Table S-2

ID	Sample	Location	Stage	Phase	Location_Phase	# Raw reads	# Deduped	# Aligned	% Align	GEO Fastq file	GEO kallisto counts file
S1	Proes_Ant_B1	Anterior	Proestrus	Early	Anterior_Early	2,669,590	1,392,774	1,038,851	74.6%	Proes_Ant_B1_R1.fastq.gz	Proes_Ant_B1_kallisto_counts.tsv
S2	Proes_Ant_B2	Anterior	Proestrus	Early	Anterior_Early	2,903,086	1,583,735	1,184,664	74.8%	Proes_Ant_B2_R1.fastq.gz	Proes_Ant_B2_kallisto_counts.tsv
S3	Proes_Post_B1	Posterior	Proestrus	Early	Posterior_Early	3,820,771	1,809,899	1,358,747	75.1%	Proes_Post_B1_R1.fastq.gz	Proes_Post_B1_kallisto_counts.tsv
S4	Proes_Post_B2	Posterior	Proestrus	Early	Posterior_Early	2,542,319	1,258,262	936,809	74.5%	Proes_Post_B2_R1.fastq.gz	Proes_Post_B2_kallisto_counts.tsv
S5	Es_Ant_B1	Anterior	Estrus	Early	Anterior_Early	3,859,515	2,015,223	1,524,157	75.6%	Es_Ant_B1_R1.fastq.gz	Es_Ant_B1_kallisto_counts.tsv
S6	Es_Ant_B2	Anterior	Estrus	Early	Anterior_Early	4,976,661	2,393,539	1,803,496	75.3%	Es_Ant_B2_R1.fastq.gz	Es_Ant_B2_kallisto_counts.tsv
S7	Es_Post_B1	Posterior	Estrus	Early	Posterior_Early	3,051,253	1,508,916	1,166,422	77.3%	Es_Post_B1_R1.fastq.gz	Es_Post_B1_kallisto_counts.tsv
S8	Es_Post_B2	Posterior	Estrus	Early	Posterior_Early	1,486,318	792,559	589,353	74.4%	Es_Post_B2_R1.fastq.gz	Es_Post_B2_kallisto_counts.tsv
S9	Metes_Ant_B1	Anterior	Metestrus	Late	Anterior_Late	1,509,395	896,284	696,932	77.8%	Metes_Ant_B1_R1.fastq.gz	Metes_Ant_B1_kallisto_counts.tsv
S10	Metes_Ant_B2	Anterior	Metestrus	Late	Anterior_Late	1,742,088	1,000,503	771,609	77.1%	Metes_Ant_B2_R1.fastq.gz	Metes_Ant_B2_kallisto_counts.tsv
S11	Metes_Post_B1	Posterior	Metestrus	Late	Posterior_Late	3,034,943	1,266,394	989,728	78.2%	Metes_Post_B1_R1.fastq.gz	Metes_Post_B1_kallisto_counts.tsv
S12	Metes_Post_B2	Posterior	Metestrus	Late	Posterior_Late	4,033,746	1,918,652	1,484,995	77.4%	Metes_Post_B2_R1.fastq.gz	Metes_Post_B2_kallisto_counts.tsv
S13	Dies_Ant_B1	Anterior	Diestrus	Late	Anterior_Late	4,403,124	2,067,053	1,605,618	77.7%	Dies_Ant_B1_R1.fastq.gz	Dies_Ant_B1_kallisto_counts.tsv
S14	Dies_Ant_B2	Anterior	Diestrus	Late	Anterior_Late	4,161,010	1,439,043	1,088,609	75.6%	Dies_Ant_B2_R1.fastq.gz	Dies_Ant_B2_kallisto_counts.tsv
S15	Dies_Post_B1	Posterior	Diestrus	Late	Posterior_Late	2,131,914	946,725	726,724	76.8%	Dies_Post_B1_R1.fastq.gz	Dies_Post_B1_kallisto_counts.tsv
S16	Dies_Post_B2	Posterior	Diestrus	Late	Posterior_Late	1,522,405	721,007	572,923	79.5%	Dies_Post_B2_R1.fastq.gz	Dies_Post_B2_kallisto_counts.tsv